

Performance of measurands in time-domain optical brain imaging: depth selectivity versus contrast-to-noise ratio

ALEH SUDAKOU,^{1,*}  LIN YANG,²  HEIDRUN WABNITZ,² 
STANISLAW WOJTKIEWICZ,¹  AND ADAM LIEBERT¹ 

¹Nalecz Institute of Biocybernetics and Biomedical Engineering Polish Academy of Sciences, Trojdena 4, 02-109 Warsaw, Poland

²Physikalisch-Technische Bundesanstalt, Abbestraße 2-12, 10587 Berlin, Germany

*asudakou@ibib.waw.pl

Abstract: Time-domain optical brain imaging techniques introduce a number of different measurands for analyzing absorption changes located deep in the tissue, complicated by superficial absorption changes and noise. We implement a method that allows analysis, quantitative comparison and performance ranking of measurands under various conditions – including different values of reduced scattering coefficient, thickness of the superficial layer, and source-detector separation. Liquid phantom measurements and Monte Carlo simulations were carried out in two-layered geometry to acquire distributions of times of flight of photons and to calculate the total photon count, mean time of flight, variance, photon counts in time windows and ratios of photon counts in different time windows. Quantitative comparison of performance was based on objective metrics: relative contrast, contrast-to-noise ratio (CNR) and depth selectivity. Moreover, the product of CNR and depth selectivity was used to rank the overall performance and to determine the optimal source-detector separation for each measurand. Variance ranks the highest under all considered conditions.

© 2020 Optical Society of America under the terms of the [OSA Open Access Publishing Agreement](#)

1. Introduction

Near-infrared spectroscopy (NIRS) is a safe and non-invasive optical tool that allows the monitoring of signals containing information about tissue optical properties in real-time at the patient's bedside. A number of clinical trials have paved the way towards a broad clinical use of NIRS today for diverse applications [1], which is highlighted by an increasing number of commercially available NIRS devices [2]. The important clinically relevant information, e.g. cerebral metabolism [3], tissue perfusion and oxygenation [4], allow to study physiological conditions and results of clinical interventions.

Functional NIRS (fNIRS) is a fast developing methodology based on the assessment of changes in the absorption coefficient of tissues related to concentration changes in oxy- and deoxy-hemoglobin. fNIRS enables the monitoring of changes in tissue oxygenation and hemodynamic changes associated with neuronal activity [5]. The method has been proven as an effective tool for neuroscience with diverse applications [6,7].

The optical signals measured on the surface of the head contain entangled information originating within the extracerebral layer, i.e. scalp and skull, and the deep layer, i.e. brain. The physiological changes in the scalp layer can mask the hemodynamic changes in the cerebral layer, which is the major cause of false-positive results in fNIRS studies [8]. As such, the effectiveness of the fNIRS method improves with increased sensitivity to brain tissue [1].

fNIRS methods can be classified as continuous wave (CW), frequency domain (FD) and time domain (TD) according to their measured signal. The current study is focused on the assessment of the effectiveness of time-domain fNIRS to detect absorption changes in the brain cortex

and reduce the contamination of the signals caused by hemoglobin concentration changes of the extracerebral tissues. We report on measurands that can be (in part) relevant for all three modalities: CW, FD and TD-NIRS. TD-NIRS uses the most sophisticated instruments and provides superior information on the propagation of light in tissue. The advances in laser and detector technologies have reduced the instrumental costs and improved the performance of measurements allowing more information to be acquired and with more compact systems [9,10].

In brain studies, the signals in TD-NIRS are acquired in diffuse reflectance geometry by emitting short pulses of light, on the order of picoseconds in width, into the tissue and measuring the arrival times of remitted photons using time-correlated single photon counting (TCSPC) electronics, which provides the distribution of times of flight of photons (DTOF). Several methods of analyzing the DTOF have been developed. The fitting method uses essentially the entire DTOF for accurate estimation of the absolute values of absorption and reduced scattering coefficients in an optically turbid, homogeneous medium [11]. On the contrary, if monitoring of absorption changes is of interest, it is beneficial to calculate a few measurands that characterize the DTOF profile. A few approaches to analyze DTOFs include Mellin-Laplace moments [12], time-dependent mean partial pathlengths (TMPP) [13] and time segmented analysis [14]. The measurands used in the present work follow the choice used by Wabnitz *et al.*, [15,16]: statistical moments (number of photons, mean time of flight and variance) [17], photon counts in time windows [18,19] and ratios of photon counts in different time windows [18,20]. Currently, there is no quantitative comparison of the various measurands that would suggest the optimal choice for the purpose of monitoring small absorption changes in the deeper layers. Furthermore, such comparison could demonstrate the features of the various measurands and thus help interpret *in-vivo* measurements.

The theoretical background of the present work was presented in previous related studies [15,16,21]. In [21] it was shown that the higher-order moments reveal higher sensitivity to changes in absorption appearing in deeper tissues. Authors of [15] introduced methods for characterizing the performance of TD-fNIRS systems to detect, localize, and quantify small absorption changes in deep tissue compartments. In the recent study [16] it was shown that the ratios of photon counts in late time windows can yield the highest depth selectivity. However, it is expected that the practical utility of these measurands can be impeded by noise as the late time windows have particularly high relative noise levels.

In the present work we extend the analyses presented in [16] to include noise, which is often a limiting factor in fNIRS measurements, and propose a metric to rank the measurands (moments of DTOFs, time windows and ratios of photon counts) in terms of their overall performance in monitoring absorption changes in the deeper (brain cortex) layer. The main aim of this work is to provide a quantitative comparison of measurands' performances, and supplement it by including the dependence on other parameters, e.g. reduced scattering coefficient, thickness of the superficial layer, and the source-detector separation. We assess the performance of the various measurands based on three objective metrics: relative contrast to absorption changes in each layer, contrast-to-noise ratio (CNR) for each layer, and depth selectivity. A desired measurand should have high contrast to absorption changes in the deeper layer and little influence from absorption changes in the superficial layer. The product of CNR for the deeper layer and depth selectivity is proposed as a metric to rank measurands in terms of their overall performance. This metric incorporates the sensitivity to the deeper layer, contamination from the superficial layer and noise relative to the signal. We carried out TD-NIRS measurements on two-layered liquid phantoms with the absorption changing in each layer separately. The analysis using simulated data were repeated for various values of reduced scattering coefficient, thickness of the superficial layer and source-detector separation.

2. Measurands

This section introduces the analytical expressions of the measurands that exploit statistical moments and time windows. These measurands were calculated from measured DTOFs and also from simulated DTOFs convolved with the experimental instrument response function (IRF). In this study, we consider a 4 ns long range of the DTOFs to calculate the measurands. Within this range the photon counts at different times in the DTOF can differ by up to 4 orders of magnitude, i.e. the background signal is 0.01% of the maximum photon count. Usually the region that has $\geq 1\%$ of the maximum photon count (2 orders of magnitude) is used for analyses of DTOFs [22], i.e. a much smaller dynamic range.

Normalized moments of order n of a distribution function can be defined by [17]:

$$m_n = \frac{\sum_{i=1}^{i_{\max}} t_i^n N_i}{\sum_{i=1}^{i_{\max}} N_i}, \quad (1)$$

where m_n is the n^{th} normalized moment, t_i is the time corresponding to time channel i , and N_i is the number of detected photons in time channel i . In particular, we focus on three statistical moments: total number of photons ($m_0 = N$), mean time of flight (m_1) and variance ($V = m_2 - m_1^2$). V is the second centralized moment, which is related to the first two moments. For the calculation of N the temporal dependence of the photon counts is not used and this measurand represents the measure of light intensity that can be obtained with continuous-wave NIRS systems.

The time windows of equal width were defined in accordance with the definition used in the nEUROpt protocol [15]. The width of 500 ps results in eight consecutive time windows within the 4 ns range. The photon count (N_k) in the k^{th} time window, between a and b time channels, is obtained by the summation:

$$N_k = \sum_{i=a}^b N_i \quad (2)$$

The ratio of the photon counts in different time windows ($N_{l/e}$) is calculated as:

$$N_{l/e} = \frac{N_l}{N_e}, \quad (3)$$

where N_l and N_e are the photon counts in later (l) and earlier (e) time windows, respectively. These ratios, similar to m_1 and V , have the potential to eliminate the influence of superficial changes on the signals, providing high sensitivity to changes appearing in the deeper regions, e.g. cerebral cortex.

3. Metrics for comparing TD-NIRS measurands

This section defines five metrics, some of which were introduced in the nEUROpt protocol [15]. They can provide comparable quantitative information about the performance of different measurands with respect to sensing of small absorption changes in layered structures.

3.1. Relative contrast

Relative contrast (C) is defined as the relative change of a measurand (M) with respect to its baseline value:

$$C_i = \frac{M_i - M_0}{M_0}, \quad (4)$$

where M_0 is the baseline value of a measurand and M_i is its value after an absorption change in layer i . Relative contrast will depend on the location, the volume and the magnitude of the absorption change and such dependence is different for different measurands, which in turn allows for various depth-resolved analyses. Relative contrast is dimensionless and hence appropriate for

comparing any measurands. However, relative contrast does not reflect the uncertainty of the measurand nor the contamination level due to unwanted absorption changes in the superficial layer.

3.2. Noise

The photon noise is the main limitation in optical *in-vivo* measurements, mainly due to the safety limitations for laser power. The standard deviation of measurands due to photon noise (σ) follows Poisson statistics and can be calculated from measured or simulated DTOF. The analytical expressions for σ of the three statistical moments were given in Liebert *et al.*, [17]. The photon counts in different time channels (N_i) are assumed to be uncorrelated, i.e. statistically independent, and the noise for each time channel is assumed to follow Poisson statistics [23]. Then, the following equations can be derived by applying the propagation of uncertainty in a similar manner as shown in Liebert *et al.*, [24]:

$$\sigma^2(N) = \sum N_i = N \quad (5)$$

$$\sigma^2(m_1) = \frac{V}{N} \quad (6)$$

$$\sigma^2(V) = \frac{m_{4,C} - V^2}{N}, \quad (7)$$

where $m_{4,C}$ is the fourth centralized moment and is related to the first four moments ($m_{4,C} = m_4 - 4m_3m_1 + 6m_2m_1^2 - 3m_1^4$). The following analytical expression is used for σ of the photon count within k^{th} time window, which contains time channels between a_k and b_k :

$$\sigma^2(N_k) = \sum_{i=a_k}^{b_k} N_i \quad (8)$$

The following analytical expression for the standard deviation of the ratios of photon counts in time windows was derived by applying the propagation of uncertainty using the photon noise within late $\sigma(N_l)$ and early $\sigma(N_e)$ time windows:

$$\sigma^2(N_{l/e}) = N_{l/e}^2 \left(\frac{\sigma(N_e)^2}{N_e^2} + \frac{\sigma(N_l)^2}{N_l^2} \right) \quad (9)$$

Note that instead of analytically calculating photon noise, it is possible to estimate the standard deviation directly from a number of repeated measurements. However, this ‘measured’ noise typically results in a higher noise level for all measurands, as it includes the instrumental noise as well. While the photon statistics remains the dominant source of noise in NIRS measurements.

3.3. Contrast-to-noise ratio

Contrast-to-noise ratio is the ratio between the change in a measurand ($M_i - M_0$), which originates from a change in absorption in layer i , and its standard deviation during baseline measurement ($\sigma(M_0)$) [15]:

$$CNR_i = \frac{M_i - M_0}{\sigma(M_0)} \quad (10)$$

Note that the definition of contrast used in CNR is different to the definition of relative contrast. σ can be calculated using Eqs. (5)–(9), which will include only photon noise, or using standard deviation of repeated measurements, which will also include instrumental noise. We assume the photon noise as the dominant source of noise and neglect the instrumental noise. CNR is dimensionless and hence appropriate for comparing different measurands. For brain studies, a good measurand should present high CNR for the deeper layer. However, CNR does not contain information about the level of contamination from the superficial layer.

3.4. Depth selectivity

Depth selectivity (S) is defined as the ratio of the relative contrasts in two layers [15]:

$$S = \frac{C_2}{C_1} = \frac{M_2 - M_0}{M_1 - M_0}. \quad (11)$$

The nominator and the denominator correspond to a change in a measurand due to an absorption change in the deeper layer ($i = 2$) and in the superficial layer ($i = 1$), respectively. For estimation of this metric, the changes in absorption in the two layers must be of equal magnitude. It reflects the sensitivity of a measurand to the deeper layer compared to the superficial layer. A higher value of S indicates the measurand will be less influenced by absorption changes in the extracerebral layer, which is helpful for imaging absorption changes in the cerebral tissue. However, this metric does not reflect the uncertainty of a measurand.

3.5. Product of depth selectivity and contrast-to-noise ratio for the deeper layer

We propose a new metric that combines the depth selectivity and the contrast-to-noise ratio in the deeper layer to give a score for the overall performance of a measurand for estimation of absorption changes in the deeper layer:

$$S \times CNR_2 = \frac{(M_2 - M_0)^2}{\sigma(M_0) \times (M_1 - M_0)}. \quad (12)$$

The product of S and CNR_2 represents a combination of sensitivity to the deeper layer, the influence of contamination from the superficial layer and the uncertainty in comparison to the contrast. This quantity is dimensionless and hence suitable for comparing performance of measurands of different units.

4. Implementation

4.1. TD-NIRS system

A supercontinuum laser FIU-15 PP (NKT Photonics) equipped with a variable bandpass filter VARIA (NKT Photonics) with a bandwidth of 10 nm was used as the light source providing picosecond light pulses with a repetition rate of 39 MHz. The filter was set to 760 nm. The output beam was guided to the phantom by a 1.6 m long multimode graded index fiber (core diameter 400 μm , NA 0.27, Leoni, Germany), and then collected by another 1.6 m long multimode graded index fiber (core diameter 600 μm , NA 0.22, Leoni, Germany). Both fibers' ends were embedded into a black fiber holder to prevent stray light and ambient light from entering the detecting fiber, and then faced the plexiglass windows of the phantom container.

A hybrid photomultiplier module (HPM-100-50, Becker & Hickl, Germany) received the light collected by the detecting fiber. A shutter, a motorized neutral-density attenuator, a collimator, and a focusing lens were placed between detecting fiber's end and detector to adapt the intensity and to properly image the detector fiber onto the detector.

The detected single-photon pulses were recorded by a time-correlated single photon counting (TCSPC) module (SPC-150, Becker & Hickl, Germany). Each DTOF contained 4096 time channels and every time channel was 4.07 ps in width. The photon counts in time windows (Eq. (2)) were calculated using the time channels inside the corresponding 500 ps time window, and the photon counts in the time channels that were on the limits were linearly interpolated.

The proper recording of the IRF is crucial for the accuracy in TD-NIRS measurements. Here the fibers were mounted into a cage system, and thin scatterers were included to engage the full aperture of both fibers [25]. The distance between the two fibers' ends (54 mm) determined the time shift between IRF and DTOF measurements.

4.2. Phantom measurements

Intrinsic optical properties of scattering and absorbing components may vary for different brands and even for different batches of scattering and absorbing components, especially so for India ink [26]. The intrinsic absorption coefficient of India ink (Higgins Ink #44201, Chartpak, USA) and the intrinsic reduced scattering coefficient of 20% Intralipid (Fresenius) were characterized in a 30 mm thick homogenous phantom container by measuring in reflectance and in transmittance geometries and applying the procedure that is described in detail in [26]. The characterization of absorption (μ_a) was carried out within the nominal values from 0 to 0.02 mm^{-1} at 750 nm with 6 stepwise changes in India ink concentrations, while the nominal value of scattering was fixed at around 1 mm^{-1} . The characterization of scattering (μ'_s) was carried out within the range from 0.5 to 1.5 mm^{-1} at 750 nm with 3 stepwise changes in 20% Intralipid concentrations, while no India ink was added.

The two-layered phantom container, described in [15,27], was used for the layered liquid phantom measurements in reflectance geometry. The front wall was 2 mm thick and contained plexiglass windows of 7 mm in diameter for the source and the detector fibers. The time light travels through the plexiglass windows is subtracted from the time of arrival of photons. The thicknesses of the two compartments were 10 and 40 mm, and they were separated by a $50 \mu\text{m}$ thick translucent Mylar foil (DuPont). The distance between the source and detector fibers was set to 30 mm. Each DTOF was measured with a collection time of 1 s and 100 repetitions. The photon count rate of single DTOFs during homogeneous measurement was kept close to $5 \times 10^5 \text{ s}^{-1}$ to prevent counting loss and shape distortions of the DTOF due to dead time effects (see Fig. 414 in [28]). Single DTOFs were used for the photon noise calculation (Eqs. (5)–(9)) and the average of 100 DTOFs was used for calculating the values of the measurands (Eqs. (1)–(3)).

The target baseline optical properties were $\mu_a = 0.01 \text{ mm}^{-1}$ and $\mu'_s = 1 \text{ mm}^{-1}$ at 760 nm. A specific solution of India ink, water and 20% Intralipid was separated in three equal parts and added to increase absorption properties in one of the compartments by a total of 15% ($\Delta\mu_a = 0.0015 \text{ mm}^{-1}$) without changing the scattering properties. Then the liquid was removed from the container, and the experiment was repeated with another solution added into the other compartment in three steps to increase the other compartment's absorption properties from baseline by a total of 15% without changing the scattering properties. Therefore, four sets of measurements were used for the present study: i) homogeneous medium before adding absorber to the superficial layer, ii) after increasing absorption in the superficial layer by 15%, iii) homogeneous medium before adding absorber to the deeper layer, and iv) after increasing absorption in the deeper layer by 15%. The protocol allows to study measurands' ability to reflect changes in the deeper layer as well as in the superficial layer.

The considered absorption changes are somewhat higher than typically observed during functional near-infrared spectroscopy (fNIRS) studies [29,30]. The higher absorption changes were chosen to obtain results with better signal-to-noise ratio with regard to intrinsic uncertainties contained in measurements and Monte Carlo simulations. The linearity regime in which the changes in the measurands have a linear dependence on the absorption changes, as discussed in [15], is commonly assumed for many methods of analyzing fNIRS measurements, e.g. [21]. The three moments of DTOFs have good linearity for up to 40% change in absorption in any of the two layers of the model (Fig. 6 in [15]). Thus, we can assume that the scenario considered in this work, i.e. 15% change in absorption in each layer, is within the linear regime.

The position of time zero, i.e. the start of the first time window, was defined as the barycenter of the measured instrument response function (IRF) in the interval between the points of half maximum [15]. IRF was measured twice, at the start and end of the experiment, and the timing drift was negligible.

4.3. Monte Carlo simulations

Monte Carlo simulations (MC) were carried out using the code that was introduced by Wojtkiewicz *et al.*, [31], which evolved from the code reported by Liebert *et al.*, [32]. The symmetry of the slab-based layered model allows positioning a ring of many detectors around a center-located source to significantly increase the detection area and proportionally decrease the computational time. The optodes arrangement is shown in Fig. 1. The radius of each circular detector was set to 1 mm. The model (200×200×80 mm) was divided into uniform cube voxels of 0.25 mm width and consisted of the superficial layer (thickness 5, 10 or 15 mm) and the deeper layer. The superficial layer thicknesses were chosen based on the typical scalp thicknesses for an adult head, e.g. as in [33]. The refractive index was set to 1.33 and the scattering was assumed to be isotropic. Three MC simulations were carried out to mimic the measurement protocol: homogeneous model with $\mu_a = 0.01 \text{ mm}^{-1}$, 15% increase in absorption in the superficial layer only, and 15% increase in absorption in the deeper layer only.

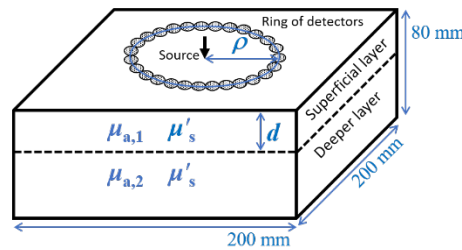


Fig. 1. The two-layered model for the Monte Carlo simulations.

MC simulations and analyses were repeated for the varying values of parameters as listed in Table 1. The first row lists the baseline optical properties for the homogeneous phantom measurements estimated with the curve fitting method [11,34] using NIRFASTER software [35]. The fitting method used the analytical solution of the radiative transfer equation under the diffusion approximation with extrapolated boundary conditions for time-resolved reflectance in a homogeneous slab. The second row lists the nominal values of baseline optical properties as used in the MC simulations. A total number of 2×10^9 and 9×10^9 photon packets were simulated for ρ up to 35 mm and for ρ larger than 35 mm, respectively. The simulated DTOFs were sampled at 700 time channels with 10 ps width. All DTOFs were convolved with the measured IRF and the first 400 time channels were used for further calculations as shown in Fig. 2(a). The three moments were calculated using this whole range and each of the eight time windows included 50 time channels.

Table 1. Model parameters used in Monte Carlo simulations and phantom data. μ'_s – reduced scattering coefficient of both layers, d – superficial layer thickness, ρ – source-detector separation. In all cases, absorption (μ_a) was increased separately within both layers by 15%.

	μ_a / mm^{-1}	μ'_s / mm^{-1}	d / mm	ρ / mm
Phantom	0.0102	1.09	10	30
Nominal	0.01	1.0	10	30
Varying μ'_s	0.01	0.5; 1.0; 1.5	10	30
Varying d	0.01	1.0	5; 10; 15	30
Varying ρ	0.01	1.0	10	10; 15; 20; 25; 30; 35; 40; 45; 50

All simulated DTOFs after convolution were scaled to match the measurement using the scaling factor, which was calculated by scaling measured and simulated curves for the homogeneous

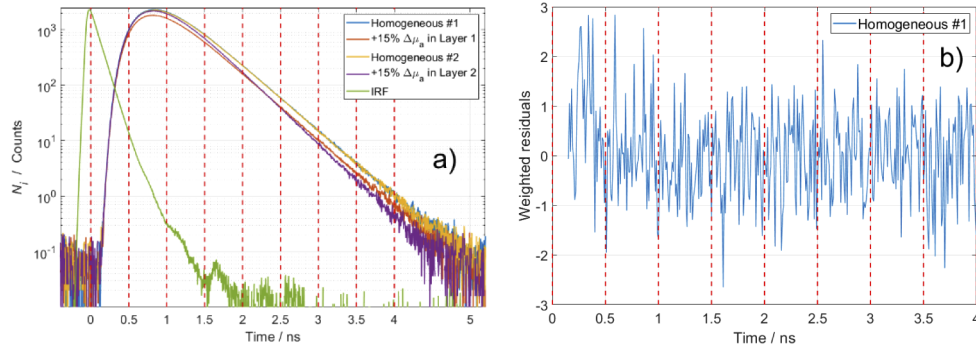


Fig. 2. (a) Measured DTOFs and IRF (both averaged over 100 repetitions) after background subtraction and correction for different time delays; time channel width is 4.07 ps. (b) Weighted residuals for comparison between a single measured DTOF and a simulated DTOF convolved with IRF for the phantom measurement parameters, which are shown in the first row of Table 1; time channel width was interpolated to 10 ps. The vertical dashed red lines show the limits of the eight time windows of 500 ps width. The range from 0 to 4 ns was used for the calculation of statistical moments.

phantom parameters (first row in Table 1). Hence, the photon noise level in results of MC simulations matches the one typically observed during *in-vivo* time-resolved measurements with a collection time of 1 s. A collection time of 1 s, which corresponds to the phantom measurement and its noise level, is adequate for monitoring hemodynamic changes in the brain. The number of collected photons, which is proportional to the collection time, has an influence on the photon noise and hence on *CNR*, while relative contrast and depth selectivity are unaffected.

5. Results and discussions

5.1. Measurements and corresponding Monte Carlo simulations

Figure 2(a) shows the measured DTOFs (averaged over 100 s) after accounting for the different time delays in the IRF and phantom measurements as explained in Section 4.2. The full width at half maximum of the measured IRF is 126 ps. The discrepancies between Monte Carlo simulations and measured DTOFs for homogeneous medium are on the level of noise, as can be verified by the weighted residuals calculated using a single DTOF and shown in Fig. 2(b). The weighted residuals for each time channel i were calculated as: $(N_{i,meas} - N_{i,sim}) / \sqrt{N_{i,sim}}$, where N_i is the number of photons in individual time channels for measurement and simulation. Only for the calculation of weighted residuals, the measured single DTOF was interpolated in time domain to increase the width of time channels from 4.07 to 10 ps to match the time channels of the simulated DTOF. This simulated DTOF, which corresponds to the homogeneous case for the phantom parameters in Table 1, was rescaled to match the integrated photon count of the homogeneous measurement, $N = 5.2 \times 10^5$, as mentioned in Section 4.3. The same scaling factor was applied to all other simulated DTOFs, which corresponds to a detection system with a fixed sensitivity. Also, the analysis for different values of source detector separation, in Section 5.4, was repeated with $N = 5 \times 10^5$ for each homogeneous measurement, which corresponds to a detection system with a varied sensitivity.

5.2. Results of the various metrics for measured and simulated data

The results of the calculations of different metrics for all measurands are presented in Fig. 3 for the measured TD-NIRS data and for the corresponding MC simulated data. All possible ratios of late and early time windows are presented.

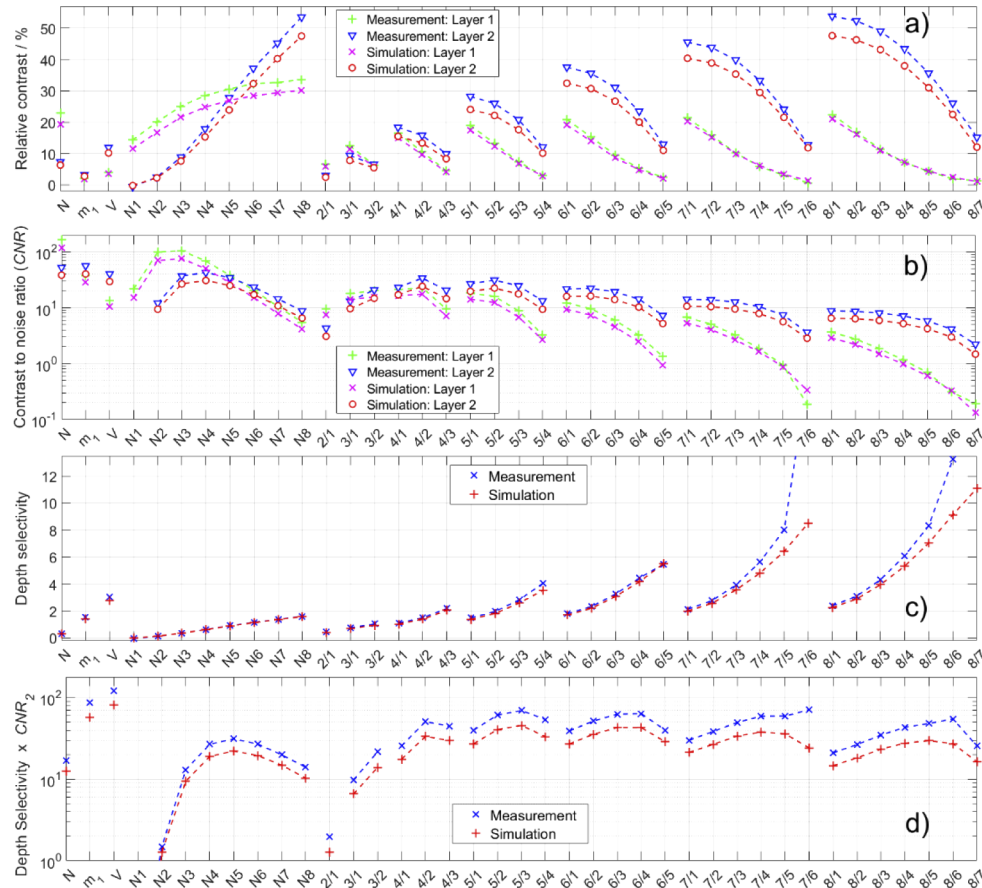


Fig. 3. Results of analysis of the various metrics obtained for moments (N , m_1 , V), photon counts in time windows (N_1 to N_8) and their ratios ($N_{2/1}$ to $N_{8/7}$). (a) Relative contrasts caused by 15% absorption changes in superficial and deeper layers separately. (b) Contrast-to-noise ratio (unitless) for each of the two layers. (c) Depth selectivity (unitless). (d) Product (unitless) of contrast-to-noise ratio for the deeper layer and depth selectivity. Simulated data correspond to the parameters listed in the first row in Table 1. Photon noise calculation was based on a total photon count $N = 5.2 \times 10^5$ and using the simulated DTOF for the homogeneous case.

The relative contrasts related to absorption changes in the superficial layer (layer 1) and in the deeper layer (layer 2) are presented in Fig. 3(a). The magnitudes of relative changes in statistical moments are up to 23%, 8% and 11% for the number of photons (N), mean time of (m_1) flight and variance (V). These changes are higher than typically seen in fNIRS measurements, but do not go beyond the linear regime [15]. In agreement with known results [15,36], N has a much higher relative contrast to changes in the superficial layer than in the deeper layer, and on the contrary V has a much higher relative contrast to changes in the deeper layer than in the superficial layer. The early time windows (N_1 and N_2) have significant relative contrast to changes in the superficial layer only, which supports the expectation that the early photons do not penetrate the deeper layer [37]. As a consequence, the results highlight that early time windows are prominent for monitoring changes in the superficial layer. For the later time windows a nearly linear increase in the relative contrast related to the deeper layer with increase of time is observed. Also, a small increase in the relative contrast related to the superficial layer with increase of

time is noted, which highlights that all time windows are highly susceptible to contamination from the superficial layer. The observed trends for the relative contrasts of time windows are in agreement with trends for the time-dependent mean partial pathlengths (TMPP), which is a sensitivity measure for individual time channels introduced by Steinbrink *et al.*, [13]. The ratios of time windows reveal lower relative contrast when changes in absorption appear in either superficial or deeper layers compared to individual time windows, and in particular $N_{7/6}$ and $N_{8/7}$ show almost no relative contrast for a 15% absorption change in the superficial layer. The ratios between early time windows (N_1 to N_4) show a poor relative contrast for the changes located in deeper layer and a similar relative contrast for the absorption changes located in the superficial layer. Hence, later time windows (N_5 and later) are essential for detecting absorption changes located in the deeper layer. The magnitudes of relative contrasts cannot be used to objectively compare different measurands without accounting for their noise, e.g. the low values of relative contrast for m_1 .

The contrast-to-noise ratios (Fig. 3(b)) for the two layers allow to quantitatively compare the contrasts with respect to the level of the associated noise for each measurand. For the first time window, the values of contrast and hence CNR_2 are close to zero, which cannot be displayed on the logarithmic graph. The CNR_2 for the statistical moments (N , m_1 and V) are higher than for any time window or ratio of time windows, and the ratios of time windows have lower CNR than single time windows. The limitation of CNR as an overall performance metric is the lack of information about the level of superficial contamination.

Depth selectivity, shown in Fig. 3(c), allows to quantitatively compare the level of superficial contamination for different measurands. Evidently, total number of photons N is highly susceptible to superficial contamination while variance of the DTOF V is less susceptible, which agrees with general knowledge [21,38]. The depth selectivity for time windows has a nearly linear dependence on time. The depth selectivity for V is significantly higher than for any time window, but the highest depth selectivity is achieved by the ratios of the latest time windows. Unfortunately, these ratios could be accurately calculated only using simulated data because of a substantial noise in the measured data.

In this study we propose a new metric to quantitatively rank various measurands with respect to their ability to monitor absorption changes in a deeper layer. The unitless product of CNR_2 and depth selectivity is presented in Fig. 3(d) for all measurands. The result for total number of photons N (16.9 using measured data and 12.5 using simulated data) is similar to the average of the results for all time windows (16.7 using measured data and 12.1 using simulated data), since N is the sum of all time windows. The values for the first two time windows and their ratio ($6.5 \cdot 10^{-3}$, 1.2 and 1.3, respectively, for simulated data) are many times lower than for other measurands, e.g. 31.3 for the 5th time window, which highlights the especially poor performance of early time windows. The value decreases for later time windows and the 5th is the optimal time window, which could not be deduced from any of the other metrics alone. The values for ratios of time windows are higher than for time windows, which suggests that ratios are superior for monitoring absorption changes in the deeper layers. The optimal ratio of time windows, which provides the highest value, uses the 5th and the 3rd time windows ($N_{5/3}$), although the values obtained for ratios with adjacent time windows are similar. A previous study compared depth selectivity only and showed evidence to prefer ratios of the latest time windows [16], whereas the current results, which incorporate photon noise, suggest that it is not always optimal to use the latest time windows because of the substantially increasing level of noise. The measurands ranked according to their product value from highest to lowest are: variance, mean time of flight, ratios of time windows, time windows, and total photon count.

For all measurands, the values of relative contrast (Fig. 3(a)) for both layers are higher for measured data than for simulated data by up to 20%, depending on the measurand. Therefore, the values of CNR as well as the product involving CNR are also higher for the measured data. This

discrepancy between results of measurements and Monte Carlo simulations can be explained by a number of measurement uncertainties, e.g. mismatch between absorption changes in the physical phantom and the MC model, uncertainty of the thickness of the superficial layer, mismatch between boundary conditions applied in the MC model and physical phantom, as well as the light reflections on the surface of the Mylar film. The differences between results for measured and simulated DTOFs do not change the findings based on the comparison of measurands.

5.3. Results of the metrics for different parameters of the model

MC simulations and the analyses were repeated for different values of parameters listed in Table 1: the reduced scattering coefficient ($\mu'_s = 0.5, 1.0, 1.5 \text{ mm}^{-1}$) for both layers of the model, thickness of the superficial layer ($d = 5, 10, 15 \text{ mm}$) and source-detector separation ($\rho = 20, 30, 40 \text{ mm}$). The analyses for these parameters are presented in Fig. 4 for relative contrast (first row), contrast-to-noise ratio for the deeper layer (CNR_2) (second row), depth selectivity (third row), and product of CNR_2 and depth selectivity (fourth row). The results for the nominal values of parameters of the model ($\mu'_s = 1.0 \text{ mm}^{-1}$, $d = 10 \text{ mm}$, $\rho = 30 \text{ mm}$) are similar to the results presented in Fig. 3. The total number of detected photons (N), which is used to calculate the photon noise, strongly depends on the values of the models' parameters. N affects the photon noise, which influences CNR and hence the product of CNR_2 and depth selectivity. However, the values of relative contrast and selectivity are independent of N .

An increase in reduced scattering coefficient (μ'_s) deteriorates the performance of all measurands as shown by evaluation of all metrics (Figs. 4(a)–4(d)). On the contrary, the relative contrast to absorption changes in the superficial layer increases for all measurands for increasing μ'_s . This effect is consistent with the general knowledge that photons travel more superficially through a medium with an increased μ'_s . All measurands are affected similarly by a change in μ'_s . However, the overall performance of time windows (Fig. 4(d)) decreases slightly more for the earlier time windows for an increased μ'_s . The optimal choice of time window is the 4th for $\mu'_s = 0.5 \text{ mm}^{-1}$ and the 5th for higher μ'_s .

The thickness of the superficial layer (d) has the most effect on the metrics for all measurands. In particular for the relative contrasts, the probability that photons visit the deeper layer decreases with d , and the behavior is opposite for the probability that photons visit the superficial layer. The values of relative contrast are similar for all time windows for an absorption change in the superficial layer when $d = 5 \text{ mm}$, which agrees with the previously demonstrated behavior of TMPPs in layers extending up to 4 mm in depth [13]. When $d = 15 \text{ mm}$ the dependence of relative contrast on time is nearly parabolic, which also agrees with the behavior of TMPPs. The optimal time window, based on Fig. 4(h), is N_4 for $d = 5 \text{ mm}$, N_5 for $d = 10 \text{ mm}$ and N_6 for $d = 15 \text{ mm}$. An increase in d worsens relatively more the performance of earlier time windows than later time windows. Therefore, later time windows are preferred for thicker d .

The influence of ρ on the measurands is shown in Figs. 4(i)–4(l). An increase in ρ improves the relative contrast for the deeper layer for statistical moments, as expected from previous studies [22], but interestingly it has almost no effect on the relative contrasts for time windows and hence for their ratios, especially for the later time windows. The observations for total number of photons N and time windows closely agree with findings by Del Bianco *et al.*, [39], where the average penetration depth and pathlength travelled in each layer for photons with the same arrival time was found to be independent of ρ (Fig. 4(i)). On the contrary, the continuous wave probability, i.e. N , was strongly dependent on ρ , as in the present work. Assuming N increases for decreasing ρ , which corresponds to a detection system with a fixed sensitivity, then CNR_2 is higher at shorter ρ for all measurands due to smaller photon noise level. With such dependence of N on ρ , for time windows the shortest ρ is preferred, which is confirmed by the product of CNR_2 and depth selectivity. To study the effect of ρ on statistical moments and in more detail on time windows, the next section contains results for a bigger range of ρ and a more thorough

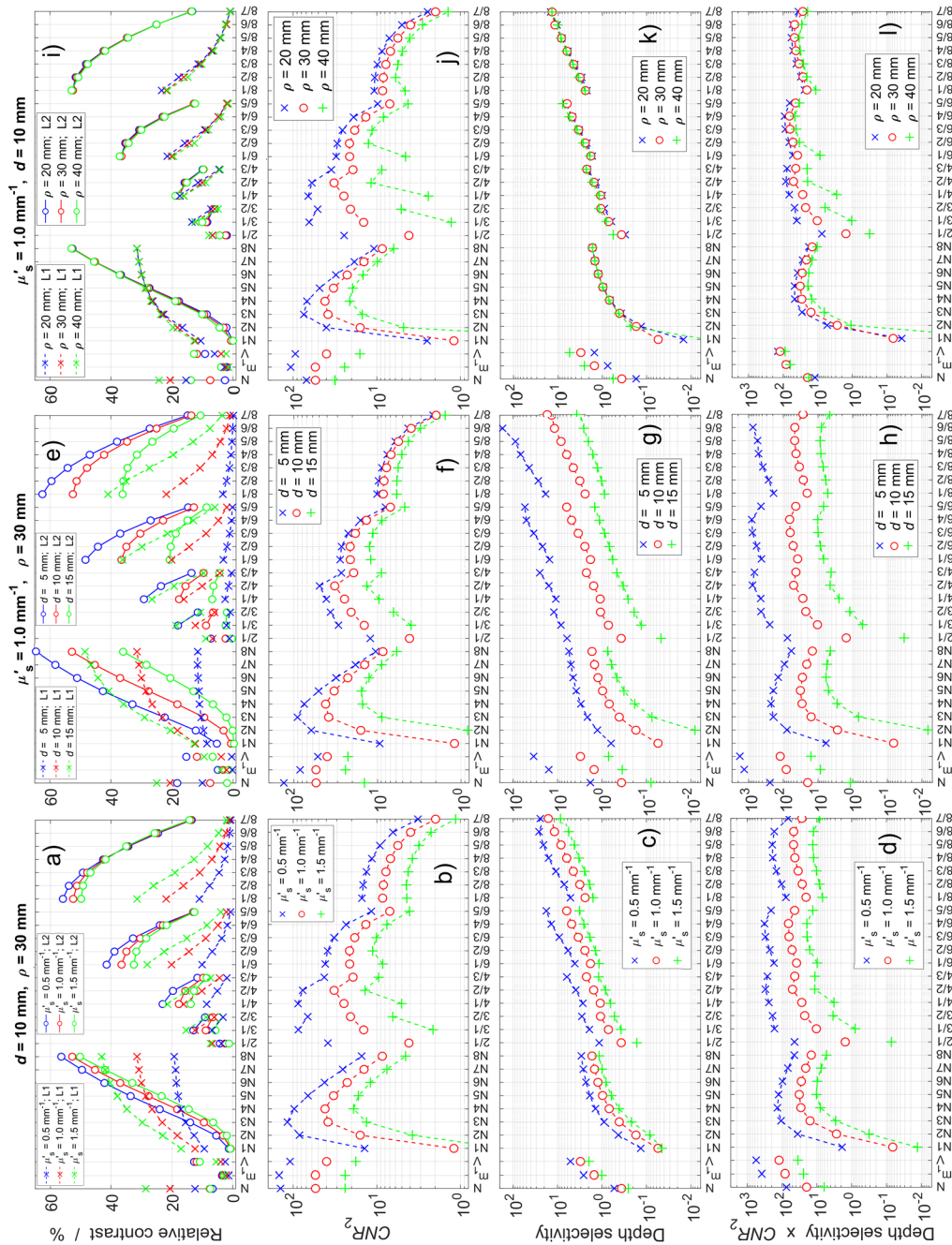


Fig. 4. Quantitative comparison of measurands using relative contrast (first row), contrast-to-noise ratio (second row), depth selectivity (third row) and product of CNR_2 and depth selectivity (fourth row) repeated for different parameters of the model: (a-d) reduced scattering coefficient (μ'_s), (e-h) thickness of superficial layer (d), and (i-l) source-detector separation (ρ). Markers with red circles correspond to the results for the nominal values ($\mu'_s = 1.0$ mm^{-1} , $d = 10$ mm, $\rho = 30$ mm), which are close to the values used for the comparison in Fig. 3. The ratios with 5th and 7th time windows in the numerator follow the trends of the ratios of other time windows, similar as in Fig. 3, and are not shown for clarity of the data presentation. Notations L1 and L2 in (a, e, i) correspond to Layer 1 and Layer 2, respectively.

analysis of the product of CNR_2 and depth selectivity. The shape of DTOFs strongly depends on the values of μ'_s and ρ . The width of time windows can be adapted to fit the whole range of a DTOF for different values of μ'_s and ρ , but it goes beyond the scope of the present study and therefore the width of time windows was kept constant (500 ps).

The presented metrics show how different parameters of the model affect the performance of measurands. Interestingly, the comparison of the product of CNR_2 and depth selectivity for different measurands has little dependence on the varied parameters of the model, and the order of measurands according to this metric remains the same: V , m_1 , ratios of time windows, time windows and N . On the contrary, the varied parameters can differently affect the values of relative contrast, CNR , and depth selectivity for the different considered measurands. The analyses for different models' parameters can help explain the possible causes for discrepancies between measurements and simulations shown in Fig. 3. A change in reduced scattering coefficient or thickness of the superficial layer changes the relative contrasts for the two layers in opposite directions. The large influence of d poses an issue for brain studies using fNIRS as the thickness of extracerebral layer is usually unknown and varies greatly between subjects. The typical thickness of the scalp and skull is around 10 to 14 mm [40,41]. As a consequence of the lack of knowledge of d , the magnitudes of observed contrasts during measurements on different patients cannot be directly compared.

5.4. Depth selectivity vs. contrast-to-noise ratio

A more informative way to analyze the product of CNR_2 and depth selectivity (fourth row in Fig. 4) is to plot CNR_2 versus depth selectivity, which is shown in Fig. 5 for different values of scattering coefficient (μ'_s) and thickness of the superficial layer (d). The similar analysis for different values of source-detector distance (ρ) is shown in Fig. 6. The graphs allow to view separately the contributions of CNR_2 and depth selectivity. The information contained in Figs. 3(b)–3(d) is shown in Fig. 5(b) for simulated data and in Fig. 5(e) for measured data.

Variance of the DTOF does not have the highest CNR_2 nor the highest depth selectivity, e.g. Figure 5(d), but its product of CNR_2 and depth selectivity is always the highest out of the considered measurands, which is shown as a dashed red line in all panels in Fig. 5. Mean time of flight (m_1) is the second best measurand. The results obtained using the simulated data (Fig. 5(b)) and using the measured data (Fig. 5(e)) have minor discrepancies. The latest time windows, e.g. N_7 and N_8 , contain very few photons (see DTOFs in Fig. 2(a)), and hence the metrics for these windows cannot be precisely calculated from measured data. For real *in vivo* measurements it is likely not feasible to use the latest time windows due to the limited number of photons collected at long times. Acquiring data with longer collection time cannot be a solution when monitoring fast absorption changes, but increasing the detection area or reducing ρ may be considered.

A detailed analysis of the influence of ρ on the ranking metric is shown in Fig. 6. We consider two possible dependencies of total number of photons N on ρ : N changes with ρ according to constant detection sensitivity (Fig. 6(a)), and a fixed value of $N = 5 \times 10^5$ is assumed for all ρ for the homogeneous medium (Fig. 6(b)). Note that depth selectivity is independent of N . In real measurements, the first scenario is unrealistic for low ρ because the detector would over-saturate and the second scenario is unrealistic for high ρ because insufficient photons can reach the detector to obtain an adequate count rate. In practice, in order to detect the late photons at short ρ the detector is made insensitive to the early times by using a gated detection scheme [42]. Depth selectivity for time windows has almost no dependence on ρ , especially for the later time windows, and on the contrary depth selectivity for total number of photons N demonstrates a strong dependence on ρ , as discussed in the previous section and found in Ref. [39].

Interestingly, m_1 and V perform significantly better than time windows and ratios of time windows for all considered values of interoptode distance ρ . The depth selectivity for all three statistical moments increases significantly with ρ , while it remains the same for time windows.

For larger ρ the depth selectivity of m_1 and V is much higher than even for the latest time window. As mentioned previously, the very late time windows are impractical measurands due to low photon counts that can be on the level of noise.

Assuming that total number of photons N depends on ρ , i.e. detection system with fixed sensitivity, then CNR_2 is worsened with increasing ρ for all measurands except N (Fig. 6(a)). On the contrary, if N is independent of ρ , i.e. detection system with varied sensitivity, then CNR_2 is improved with increasing ρ for all measurands (Fig. 6(b)). Using the introduced method for plotting the product of CNR_2 and depth selectivity, the optimal choice of ρ can be easily determined for any measurand. The optimal choice of ρ strongly depends on how N depends on ρ . For the case when N changes with ρ and for an ideal detector that can detect at any count rate, i.e. over-saturation of the detection system is not considered, the optimal ρ for measuring changes in N , m_1 and V are between 30 and 35 mm, at 25 mm, and at 20 mm, respectively (Fig. 6(a)). The most commonly used ρ for NIRS measurements on the human head is 30 mm, which allows to collect sufficient number of photons and avoid oversaturation of detectors. These optimal values of ρ are pertaining for the thickness $d = 10$ mm and they can differ significantly for other

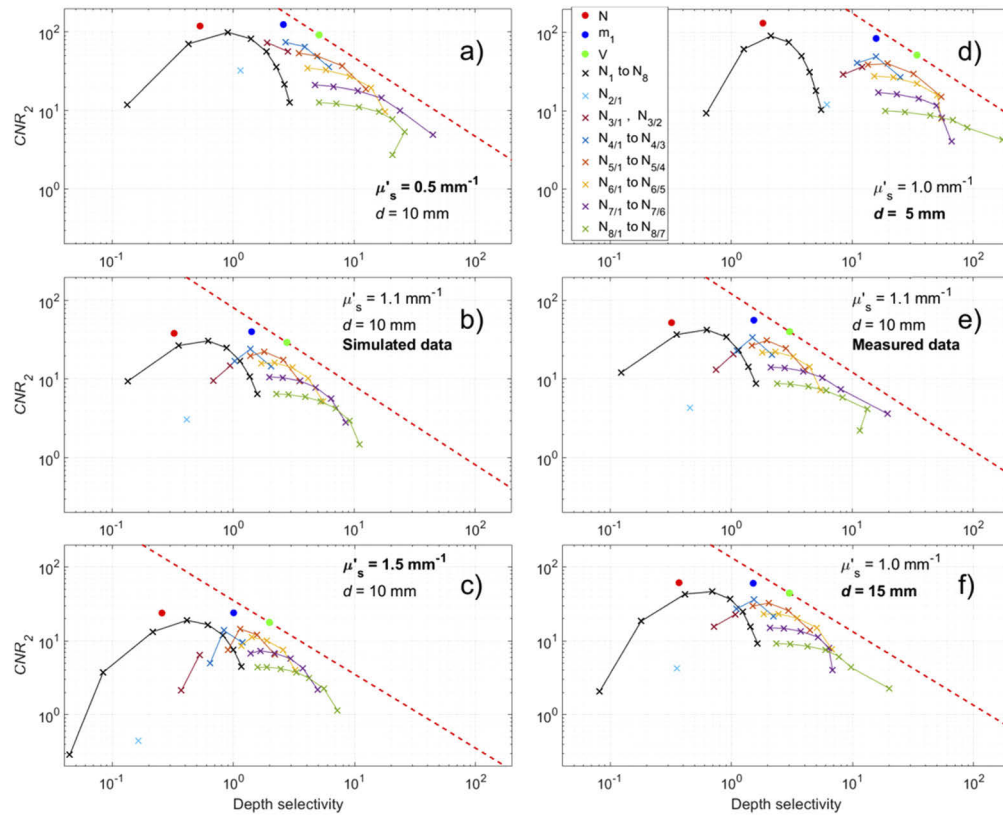


Fig. 5. Contrast-to-noise ratio for the deeper layer CNR_2 plotted against depth selectivity for all considered measurands. The analyses of data obtained by MC simulations were repeated for different values of reduced scattering (μ'_s) (a,b,c), and thickness of superficial layer (d) (d,b,f). The results obtained using simulated data (b) agree with the results obtained using measured data (e). In each panel, the dashed red line shows the value of the product of CNR_2 and depth selectivity for variance of the DTOF. Time windows (N_1 to N_8) and ratios of different time windows ($N_{2/1}$ to $N_{8/7}$) can be distinguished according to their depth selectivity, cf. Figure 3(c) and Figs. 4(c), 4(g), and 4(k).

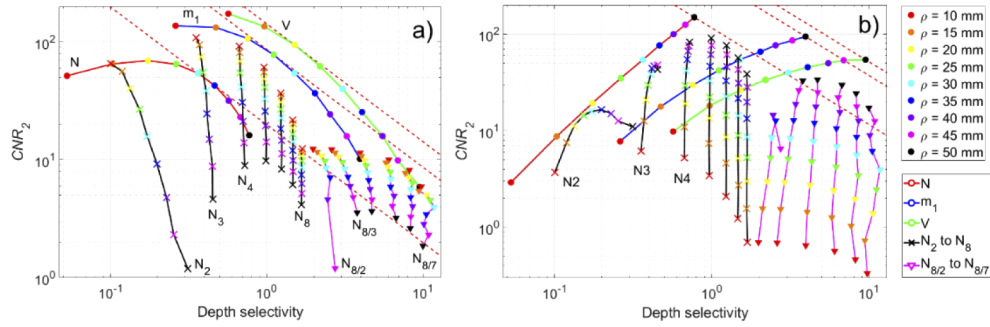


Fig. 6. CNR_2 vs. depth selectivity for various source-detector distances ρ , from 10 mm to 50 mm, and color-coded according to legend. (a) Total number of photons (N) for the homogeneous medium was assumed to change with ρ , which corresponds to measurements with a fixed detection sensitivity. (b) $N = 5 \times 10^5$ was assumed for the homogeneous medium for all values of ρ . Note that depth selectivity (x-axis) is independent of N for all measurands. The dashed red lines show the highest product of CNR_2 and depth selectivity, which correspond to the optimal choice of ρ , for N , m_1 and V . The thickness of the superficial layer was 10 mm. The values of depth selectivity for the 1st time window (N_1) are close to zero and are not displayed on the logarithmic graph. The ratios with the 8th time window in the numerator ($N_{8/2}$ to $N_{8/7}$) were chosen for display and for clarity of the data presentation; the results for other ratios have similar dependence on ρ .

values of d , which was not studied. Mean time of flight and especially variance of the DTOF are identified as the best measurands for estimating absorption changes in the deeper layer for all values of ρ between 10 and 50 mm.

6. Discussion

We carried out the quantitative comparison of the performance of measurands calculated from measured and simulated TD-NIRS data: number of photons (N), mean time of flight, variance of DTOF, photon counts in time windows and ratios of photon counts in different time windows. Measurands' ability to monitor absorption changes in the deeper layer were compared using relative contrast, contrast-to-noise ratio (CNR_2) and depth selectivity. The observed trends of measurands agree with the findings of previous studies [16,39]. However, the combination of all metrics is relevant and any single one of them is not sufficient to identify the measurand with the best overall performance. Therefore, we introduced the product of CNR_2 and depth selectivity for ranking measurands. The analyses were repeated for different reduced scattering coefficient, thickness of the superficial layer and source-detector separation (ρ), which also allowed us to determine the optimal choice of ρ for each measurand assuming the two dependencies of total number of collected photons N on ρ .

One of the findings of our study is that variance has the highest value of the product of CNR_2 and depth selectivity for all considered values of parameters of the model and for both assumptions of how N depends on ρ . This finding suggests that it is the best measurand for monitoring absorption changes in the deeper layers, despite the fact that variance does not have the highest value for any of the single evaluated metrics. It should be noted that N has a major influence on the photon noise and CNR , but the qualitative comparison and ranking of measurands is independent of N .

When N is assumed to be independent of ρ , an increase in ρ improves performance for all measurands. When N changes with ρ , the optimal ρ values are between 30 and 35 mm for N ,

25 mm for m_1 and 20 mm for V . The shortest ρ is preferred for time windows method due to the highest N , neglecting the possibility of oversaturation.

The influence of IRF can have substantial consequences for measurands based on time windows [16]. However, the experimental IRF that is relevant in the present study has a clean shape with a fast, nearly exponential decay and no after-pulsing background, no slow tail and no afterpeaks. Such shape implicates little influence on the time-window measurands [15,16].

The depth selectivity shows that time windows and their ratios can be sensitive to absorption changes appearing at different depths, which suggests that they contain the most information about absorption changes in different layers. The higher photon noise associated with late time windows is the consequence of using fewer photons in their calculations compared to earlier time windows as well as to statistical moments. The study and optimization of measurands with the aim to retrieve the most information about deep absorption changes have been addressed previously [24]. The new methods for quantitative comparison facilitate further advancements in optimization of measurands.

The current work outlines the methodology for quantitatively comparing different measurands' performances, as available in time-domain, frequency-domain and continuous-wave fNIRS signals analyses, for detecting the absorption changes in the deep tissues, e.g. brain. The methodology was applied to the well-defined two-layered geometry, which is an easy to manipulate and understand analog of a human head [43], to highlight the expected behaviors of measurands as well as to show their ranking in a fully controlled measurement configuration. The adult head is commonly simplified as a homogeneous (or two-layered) model [43]. Therefore, the findings for a two-layered model could be applicable to brain measurements. Methodology as presented in this work can be further expanded by analyses of more realistic tissue composition e.g. to study the effect of cerebrospinal fluid, skull microcirculation, or analyses of influence of layers thicknesses. fNIRS measurements can be carried out on an adult head, or on neonates (who have very different thicknesses of tissue layers compared to adults), or on muscles under a layer of skin and fat. The proposed methodology can be applied to more realistic models (e.g. MRI-based head or thyroid).

7. Conclusions

The concepts used in this work were built upon previous studies [15,16], but were extended to include noise in the assessment of performance and provide an objective metric (CNR_2) for ranking of measurands in terms of their overall performance. The product of CNR_2 and depth selectivity that was applied to various scenarios turned out to yield a valid overall performance measure. It can be included in the future for performance characterization and comparison of NIRS measurands calculated from measured or simulated data in time domain or other domains.

We found that variance always (regardless of photon count noise, scattering coefficient, superficial layer thickness, and source-detector separation) has the highest overall performance compared to other measurands i.e. total number of photons, mean time of flight, time windows, and ratios of time windows.

Funding

Horizon 2020 Framework Programme (675332 (BitMap)); Narodowe Centrum Nauki (UMO-2014/15/B/ST7/05276, UMO-2019/33/N/ST7/02918).

Acknowledgments

This project has received funding from the European Union's Horizon 2020 Marie Skłodowska-Curie Innovative Training Networks (ITN-ETN) programme, under grant agreement no 675332,

BitMap, and from The National Science Centre (NCN), Poland, under grant agreement no (UMO-2019/33/N/ST7/02918, UMO-2014/15/B/ST7/05276).

Disclosures

The authors declare no conflicts of interest.

References

1. F. Lange and I. Tachtsidis, "Clinical Brain Monitoring with Time Domain NIRS: A Review and Future Perspectives," *Appl. Sci.* **9**(8), 1612 (2019).
2. M. Smith, "Shedding light on the adult brain: a review of the clinical applications of near-infrared spectroscopy," *Philos. Trans. R. Soc., A* **369**(1955), 4452–4469 (2011).
3. G. Bale, C. Elwell, and I. Tachtsidis, "From Jöbsis to the present day: a review of clinical near-infrared spectroscopy measurements of cerebral cytochrome-c-oxidase," *J. Biomed. Opt.* **21**(9), 091307 (2016).
4. T. Hamaoka and K. K. McCully, "Review of early development of near-infrared spectroscopy and recent advancement of studies on muscle oxygenation and oxidative metabolism," *J. Physiol. Sci.* **69**(6), 799–811 (2019).
5. M. Wolf, M. Ferrari, and V. Quaresima, "Progress of near-infrared spectroscopy and topography for brain and muscle clinical applications," *J. Biomed. Opt.* **12**(6), 062104 (2007).
6. M. A. Yücel, J. J. Selb, T. J. Huppert, M. A. Franceschini, and D. A. Boas, "Functional Near Infrared Spectroscopy: Enabling routine functional brain imaging," *Curr. Opin. Biomed. Eng.* **4**, 78–86 (2017).
7. M. Ferrari and V. Quaresima, "A brief review on the history of human functional near-infrared spectroscopy (fNIRS) development and fields of application," *NeuroImage* **63**(2), 921–935 (2012).
8. I. Tachtsidis and F. Scholkmann, "False positives and false negatives in functional near-infrared spectroscopy: issues, challenges, and the way forward," *Neurophotonics* **3**(3), 031405 (2016).
9. A. Torricelli, D. Contini, A. Pifferi, M. Caffini, R. Re, L. Zucchelli, and L. Spinelli, "Time domain functional NIRS imaging for human brain mapping," *NeuroImage* **85**(Pt 1), 28–50 (2014).
10. Y. Yamada, H. Suzuki, and Y. Yamashita, "Time-Domain Near-Infrared Spectroscopy and Imaging: A Review," *Appl. Sci.* **9**(6), 1127 (2019).
11. S. Mosca, P. Lanka, N. Stone, S. Konugolu Venkata Sekar, P. Matousek, G. Valentini, and A. Pifferi, "Optical characterisation of porcine tissues from various organs in the 650–1100 nm range using time-domain diffuse spectroscopy," *Biomed. Opt. Express* **11**(3), 1697–1706 (2020).
12. A. Puszka, L. Herve, A. Planat-Chretien, A. Koenig, J. Derouard, and J. M. Dinten, "Time-domain reflectance diffuse optical tomography with Mellin-Laplace transform for experimental detection and depth localization of a single absorbing inclusion," *Biomed. Opt. Express* **4**(4), 569–583 (2013).
13. J. Steinbrink, H. Wabnitz, H. Obrig, A. Villringer, and H. Rinneberg, "Determining changes in NIR absorption using a layered model of the human head," *Phys. Med. Biol.* **46**(3), 879–896 (2001).
14. C. Sato, M. Shimada, Y. Tanikawa, and Y. Hoshi, "Estimating the absorption coefficient of the bottom layer in four-layered turbid mediums based on the time-domain depth sensitivity of near-infrared light reflectance," *J. Biomed. Opt.* **18**(9), 097005 (2013).
15. H. Wabnitz, A. Jelzow, M. Mazurenka, O. Steinkellner, R. Macdonald, D. Milej, N. Zolek, M. Kacprzak, P. Sawosz, R. Maniewski, A. Liebert, S. Magazov, J. Hebden, F. Martelli, P. Di Ninni, G. Zaccanti, A. Torricelli, D. Contini, R. Re, L. Zucchelli, L. Spinelli, R. Cubeddu, and A. Pifferi, "Performance assessment of time-domain optical brain imagers, part 2: nEUROpt protocol," *J. Biomed. Opt.* **19**(8), 086012 (2014).
16. H. Wabnitz, D. Contini, L. Spinelli, A. Torricelli, and A. Liebert, "Depth-selective data analysis for time-domain fNIRS: moments vs. time windows," *Biomed. Opt. Express* **11**(8), 4224–4243 (2020).
17. A. Liebert, H. Wabnitz, D. Grosenick, M. Moller, R. Macdonald, and H. Rinneberg, "Evaluation of optical properties of highly scattering media by moments of distributions of times of flight of photons," *Appl. Opt.* **42**(28), 5785–5792 (2003).
18. J. Selb, J. J. Stott, M. A. Franceschini, A. G. Sorensen, and D. A. Boas, "Improved sensitivity to cerebral hemodynamics during brain activation with a time-gated optical system: analytical model and experimental validation," *J. Biomed. Opt.* **10**(1), 011013 (2005).
19. L. Zucchelli, D. Contini, R. Re, A. Torricelli, and L. Spinelli, "Method for the discrimination of superficial and deep absorption variations by time domain fNIRS," *Biomed. Opt. Express* **4**(12), 2893–2910 (2013).
20. D. Contini, L. Spinelli, A. Torricelli, A. Pifferi, and R. E. D. C. R. Cubeddu, "Novel method for depth-resolved brain functional imaging by time-domain NIRS," in *Diffuse Optical Imaging of Tissue* (Optical Society of America, 2007), p. 6629_7.
21. A. Liebert, H. Wabnitz, J. Steinbrink, H. Obrig, M. Möller, R. Macdonald, A. Villringer, and H. Rinneberg, "Time-Resolved Multidistance Near-Infrared Spectroscopy of the Adult Head: Intracerebral and Extracerebral Absorption Changes from Moments of Distribution of Times of Flight of Photons," *Appl. Opt.* **43**(15), 3037–3047 (2004).
22. A. Gerega, D. Milej, W. Weigl, M. Kacprzak, and A. Liebert, "Multiwavelength time-resolved near-infrared spectroscopy of the adult head: Assessment of intracerebral and extracerebral absorption changes," *Biomed. Opt. Express* **9**(7), 2974 (2018).

23. J. Philip and K. Carlsson, "Theoretical investigation of the signal-to-noise ratio in fluorescence lifetime imaging," *J. Opt. Soc. Am. A* **20**(2), 368–379 (2003).
24. A. Liebert, H. Wabnitz, and C. Elster, "Determination of absorption changes from moments of distributions of times of flight of photons: optimization of measurement conditions for a two-layered tissue model," *J. Biomed. Opt.* **17**(5), 057005 (2012).
25. A. Liebert, H. Wabnitz, D. Grosenick, and R. Macdonald, "Fiber dispersion in time domain measurements compromising the accuracy of determination of optical properties of strongly scattering media," *J. Biomed. Opt.* **8**(3), 512 (2003).
26. L. Spinelli, M. Botwicz, N. Zolek, M. Kacprzak, D. Milej, P. Sawosz, A. Liebert, U. Weigel, T. Durduran, F. Foschum, A. Kienle, F. Baribeau, S. Leclair, J. P. Bouchard, I. Noiseux, P. Gallant, O. Mermut, A. Farina, A. Pifferi, A. Torricelli, R. Cubeddu, H. C. Ho, M. Mazurenka, H. Wabnitz, K. Klauenberg, O. Bodnar, C. Elster, M. Benazech-Lavoue, Y. Berube-Lauziere, F. Lesage, D. Khoptyar, A. A. Subash, S. Andersson-Engels, P. Di Ninni, F. Martelli, and G. Zaccanti, "Determination of reference values for optical properties of liquid phantoms based on Intralipid and India ink," *Biomed. Opt. Express* **5**(7), 2037–2053 (2014).
27. F. Martelli, P. Ninni, G. Zaccanti, D. Contini, L. Spinelli, A. Torricelli, R. Phd, H. Wabnitz, M. Mazurenka, R. Macdonald, A. Sassaroli, and A. Pifferi, "Phantoms for diffuse optical imaging based on totally absorbing objects, part 2: Experimental implementation," *J. Biomed. Opt.* **19**(7), 076011 (2014).
28. B. H. GmbH, "The bh TCSPC Handbook," User Handbook, 8th edition, www.becker-hickl.com (2019).
29. D. Contini, A. Torricelli, A. Pifferi, L. Spinelli, F. Paglia, and R. Cubeddu, "Multi-channel time-resolved system for functional near infrared spectroscopy," *Opt. Express* **14**(12), 5418–5432 (2006).
30. R. Re, D. Contini, M. Caffini, L. Spinelli, and A. Torricelli, "A compact time-resolved system for near infrared spectroscopy based on wavelength space multiplexing," *Rev. Sci. Instrum.* **81**(11), 113101 (2010).
31. S. Wojtkiewicz and A. Liebert, "Parallel, multipurpose Monte Carlo code for simulation of light propagation in segmented tissues," Manuscript submitted for publication (2020).
32. A. Liebert, H. Wabnitz, N. Zolek, and R. Macdonald, "Monte Carlo algorithm for efficient simulation of time-resolved fluorescence in layered turbid media," *Opt. Express* **16**(17), 13188–13202 (2008).
33. M. Doulgerakis, A. Eggebrecht, and H. Dehghani, "High-density functional diffuse optical tomography based on frequency-domain measurements improves image quality and spatial resolution," *Neurophotonics* **6**(03), 1 (2019).
34. M. S. Patterson, B. Chance, and B. C. Wilson, "Time resolved reflectance and transmittance for the noninvasive measurement of tissue optical properties," *Appl. Opt.* **28**(12), 2331–2336 (1989).
35. H. Dehghani, M. E. Eames, P. K. Yalavarthy, S. C. Davis, S. Srinivasan, C. M. Carpenter, B. W. Pogue, and K. D. Paulsen, "Near infrared optical tomography using NIRFAST: Algorithm for numerical model and image reconstruction," *Commun. Numer. Meth. Eng.* **25**(6), 711–732 (2009).
36. A. Gereg, D. Milej, W. Weigl, N. Zolek, P. Sawosz, R. Maniewski, and A. Liebert, "Multi-wavelength time-resolved measurements of diffuse reflectance: phantom study with dynamic inflow of ICG," in *Biomedical Optics and 3-D Imaging* (Optical Society of America, 2012), p. JM3A.31.
37. A. Pifferi, D. Contini, A. Dalla Mora, A. Farina, L. Spinelli, and A. Torricelli, "New frontiers in time-domain diffuse optics, a review," *J. Biomed. Opt.* **21**(9), 091310 (2016).
38. H. Wabnitz, M. Moeller, A. Liebert, H. Obrig, J. Steinbrink, and R. Macdonald, "Time-resolved near-infrared spectroscopy and imaging of the adult human brain," *Adv. Exp. Med. Biol.* **662**, 143–148 (2010).
39. S. Del Bianco, F. Martelli, and G. Zaccanti, "Penetration depth of light re-emitted by a diffusive medium: Theoretical and experimental investigation," *Phys. Med. Biol.* **47**(23), 4131–4144 (2002).
40. P. Sawosz, S. Wojtkiewicz, M. Kacprzak, W. Weigl, A. Borowska-Solonyanko, P. Krajewski, K. Bejm, D. Milej, B. Ciszek, R. Maniewski, and A. Liebert, "Human skull translucency: Post mortem studies," *Biomed. Opt. Express* **7**(12), 5010–5020 (2016).
41. J. D. Veesa and H. Dehghani, "Hyper-spectral Recovery of Cerebral and Extra-Cerebral Tissue Properties Using Continuous Wave Near-Infrared Spectroscopic Data," *Appl. Sci.* **9**(14), 2836 (2019).
42. L. Di Sieno, H. Wabnitz, A. Pifferi, M. Mazurenka, Y. Hoshi, A. Dalla Mora, D. Contini, G. Boso, W. Becker, F. Martelli, A. Tosi, and R. Macdonald, "Characterization of a time-resolved non-contact scanning diffuse optical imaging system exploiting fast-gated single-photon avalanche diode detection," *Rev. Sci. Instrum.* **87**(3), 035118 (2016).
43. J. Selb, T. M. Ogden, J. Dubb, Q. Fang, and D. A. Boas, "Comparison of a layered slab and an atlas head model for Monte Carlo fitting of time-domain near-infrared spectroscopy data of the adult head," *J. Biomed. Opt.* **19**(1), 016010 (2014).